Delayed Stormflow Generation in a Semi-humid Forested Watershed Controlled by Soil Water Storage and Groundwater

Zhen Cui, Fuqiang Tian[*]

Department of Hydraulic Engineering, State Key Laboratory of Hydroscience and Engineering, Tsinghua University, Beijing 100084, China.

Corresponding author: Fuqiang Tian (tianfq@tsinghua.edu.cn)

Key Points:

- Threshold dynamics between soil water content and groundwater levels govern delayed stormflow generation.

- Groundwater fluctuations regulate the timing, magnitude, and merging of delayed and direct stormflow peaks.

- Hydrological connectivity and hydraulic conductivity increase with rising groundwater levels, driving delayed stormflow.

Abstract

Recent research by Cui et al. (2024) identified a distinct threshold governing bimodal rainfall-runoff events in a semi-humid mountainous forested watershed in North China, where delayed stormflow appeared to be influenced by shallow groundwater dynamics. Building on these findings, this study delves deeper into the mechanisms driving these bimodal events, focusing on the interactions between soil water content (SWC) and groundwater level (GWL) during storm events. The results show that delayed stormflow is primarily governed by the interplay between SWC and GWL. Delayed stormflow is initiated when SWC exceeds the soil's water storage capacity, while its timing and magnitude further modulated by GWL fluctuations. During rainfall, SWC increases rapidly but stabilizes after the rain ceases if the soil's water-holding capacity is not reached. Conversely, when SWC surpasses the storage capacity, the excess rainwater infiltrates into the subsurface, recharging groundwater and causing a gradual rise in GWL. As GWL rises, enhanced hydraulic conductivity facilitates the lateral movement of shallow groundwater toward the stream channel, generating delayed stormflow. Concurrently, the effective connectivity between the stream channel and adjacent hillslopes increases in the vertical dimension. At higher GWL thresholds, GWL responses across the watershed become synchronized, significantly boosting groundwater discharge and reducing lag times. In extreme cases, the delayed stormflow peak converges with the direct stormflow peak. These findings advance the understanding of delayed stormflow mechanisms in semi-humid mountainous watersheds, contributing to refining runoff generation theories by providing insights into the threshold-driven processes that govern the timing and volume of delayed stormflow.

Keywords: Delayed stormflow; Soil water storage; Groundwater outflow; Stormflow generation mechanism; Hydraulic conductivity

1. Introduction

Stormflow processes in the Xitaizi Experimental Watershed (XEW), located in North China, exhibit a frequent occurrence of bimodal stormflow hydrographs (Fig. A1), which often lead to

2

significant stormflow and associated localized inundation. Analysis of 15 such events over the past decade revealed that the onset of these bimodal hydrographs is governed by threshold behavior. Specifically, delayed streamflow peaks tend to emerge when the combined total of event rainfall and antecedent soil moisture index exceeds 200 mm. The authors' findings suggest that shallow groundwater contributions are primarily responsible for these delayed stormflow events (Cui et al., 2024). However, the mechanisms behind the development of these bimodal hydrographs, which represent complex emergent hydrological behaviors, remain poorly understood. Understanding the formation of delayed stormflow is critical for advancing our comprehension of runoff generation processes and improving flood forecasting.

Bimodal hydrographs, characterized by dual streamflow peaks, typically occur during the wetting-up phases of catchments. Extensive research has identified several factors that influence dual streamflow peaks, including antecedent soil moisture, antecedent precipitation, groundwater levels, soil water storage, and rainfall amount (Haga et al., 2005; Graeff et al., 2009; Anderson and Burt, 1978; Padilla et al., 2015; Martínez-Carreras et al., 2016). Despite these advancements, the specific mechanisms that lead to threshold behavior and how these mechanisms produce the diverse shapes of stormflow hydrographs are still inadequately explained. For instance, Martínez-Carreras et al. (2016) found that a delayed peak only occurred when watershed storage reached a critical threshold of 113 mm. However, the precise reasons for this threshold and the underlying processes remain unclear.

The occurrence of bimodal hydrograph reflects a nonlinear runoff response, which offers valuable insights into the complex interactions between rainfall and runoff. Nonlinear pattern, including both the timing and magnitude of the response. Recent decades have seen an increase in research on nonlinear and threshold changes in rainfall-runoff responses, contributing to a deeper understanding of stormflow generation mechanisms. Nonlinear patterns, often characterized by rapid runoff responses that may lead to flooding, have been extensively documented in recent decades (Detty and McGuire, 2010; Farrick and Branfireun, 2014; Graham et al., 2010; Tromp-van Meerveld and McDonnell, 2006a; Penna et al., 2011; Scaife et al., 2020). However, many studies fail to explore

69   the intricate post-threshold mechanisms of these nonlinear shifts, leaving a gap in our understanding

70   of stormflow generation across various catchments. While threshold behaviors are widely recognized,

71   the detailed processes governing these shifts and their subsequent runoff dynamics remain

72   underexplored.

73   Bimodal stormflow responses present an opportunity to investigate the relationship between

74   rainfall thresholds and runoff generation, offering new perspectives on the timing and variability of

75   stormflow. Despite this, many studies fail to distinguish between unimodal and bimodal streamflow

76   responses. For example, Detty and McGuire (2010) focused on hydrological threshold responses but

77   did not differentiate between unimodal and bimodal hydrographs, as their study primarily addressed

78   general nonlinear rainfall-runoff processes in general. Similarly, Martínez-Carreras et al. (2016)

79   observed delayed peaks but did not further classify streamflow responses due to their focus on overall

80   watershed storage conditions. Such limitations often arise because the second peak in bimodal

81   responses typically occurs after the rainfall event has ended, whereas many studies focus on

82   streamflow changes during the event itself. Additionally, bimodal responses are influenced by

83   catchment-specific topography and geology, making them less observable in certain regions. These

84   challenges highlight the need for more in-depth investigation into bimodal streamflow responses to

85   enhance our understanding of their mechanisms. Therefore, an in-depth investigation into the

86   mechanisms driving these responses is essential. Such research would enable the grouping of similar

87   hydrologic responses and facilitate comparisons of stormflow generation processes across different

88   watersheds (Graham and McDonnell, 2010; Tromp-van Meerveld and McDonnell, 2006a, b).

89   Extensive studies across diverse regions have explored the role of soil water content and

90   groundwater levels in generating delayed peaks in stormflow. Detty and McGuire (2010) emphasized

91   subsurface flow thresholds in a forested catchment in the USA, while Farrick and Branfireun (2014)

92   analyzed soil moisture and groundwater interactions in Canadian wetlands. Penna et al. (2011)

93   examined antecedent soil moisture and storage thresholds in alpine catchments in New Zealand.

94   These studies, along with others from regions such as Japan (Haga et al., 2005) and Europe (Graeff

95   et al., 2009), contribute to the growing body of knowledge on threshold behavior in stormflow

96 responses. However, while these studies highlight the occurrence of thresholds, the complex

97 interactions that drive post-threshold runoff processes remain insufficiently understood.

98 Investigating stormflow events in semi-humid regions, such as XEW, is challenging due to the

99 relatively arid climate and low runoff coefficients. Over nearly a decade, 95 storm events were

100 identified and analyzed in XEW, offering a rare and valuable dataset for examining bimodal

101 stormflow responses in such regions. This study builds on prior findings to uncover the processes

102 underlying delayed stormflow patterns. The primary objectives of this study are: (1) to analyze the

103 temporal dynamics of soil water content (SWC) and groundwater level (GWL) during storm events,

104 (2) to elucidate the mechanisms driving the threshold behavior observed in bimodal hydrographs, and

105 (3) to reveal the underlying processes responsible for delayed stormflow in XEW.

106 **2. Materials and methods**

107 **2.1 Study site**

108 The study was conducted in the Xitaizi Experimental Watershed (XEW), a 4.22 km² catchment

109 located in North China (40°32′N, 116°37′E), approximately 70 km northeast of Beijing at (Fig. 1).

110 The watershed's elevation ranges from 676 to 1201 m above sea level, and the region experiences a

111 monsoon-influenced semi-humid climate. The average annual precipitation is 625 mm, with 80%

112 concentrated between June and September. The mean annual temperature is 11.5°C with an average

113 relative humidity of 59.1%. Forests cover 98% of the watershed, with broad-leaved species and

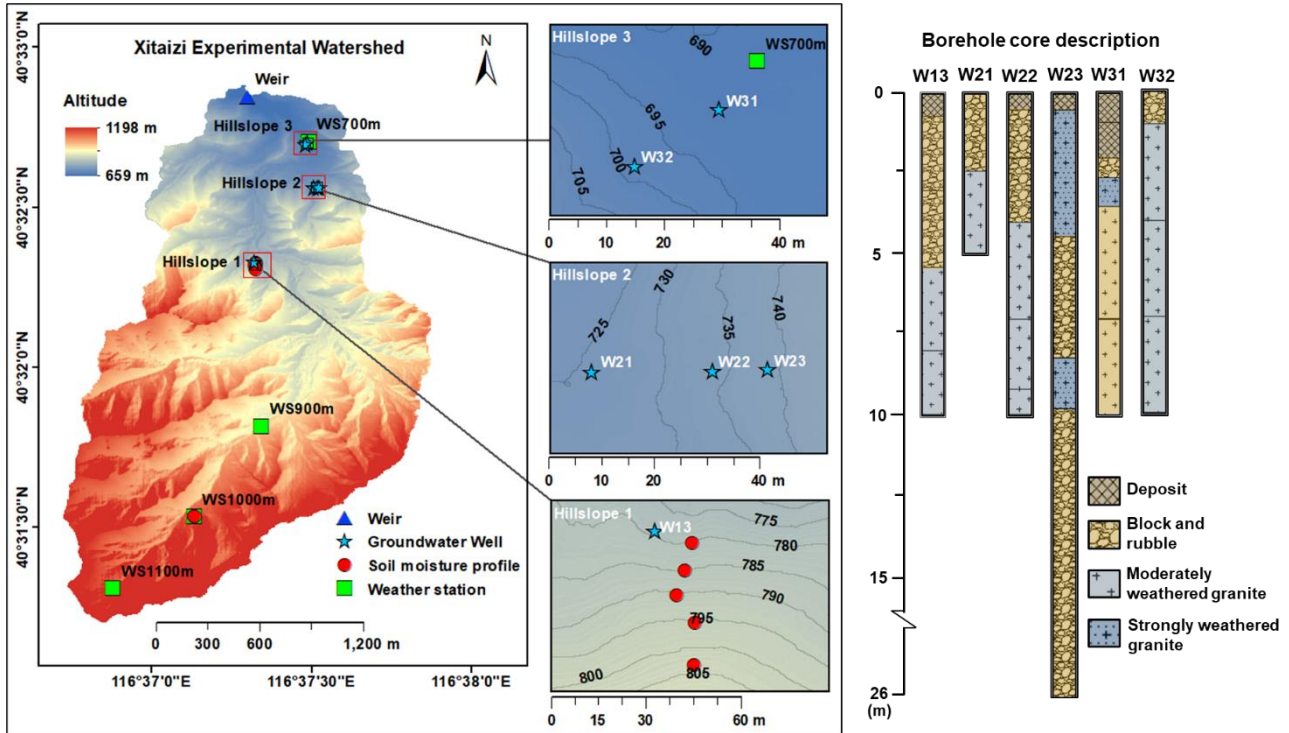114 shrubberies accounting for 54.2% and 33.0%, respectively.

Figure 1. Location of Xitaizi Experimental Watershed (XEW) and a simple description of the borehole cores. This figure shows the distribution of monitoring instruments, including four weather stations (WS700, WS900, WS1000, and WS1100), an outlet weir, six groundwater observation wells, and eight soil moisture observation profiles. Of the eight soil moisture profiles, five are located on Hillslope 1, while the remaining three are positioned on the slope near WS1000. Research hillslopes (Hillslope 1, Hillslope 2, and Hillslope 3) are delineated as key zones for hydrological and geological investigations.

The soils in XEW are primarily brown earth and cinnamon soils, with depths up to 1.5 m and an average saturated hydraulic conductivity of 45 mm/h. The surface soil is rich in organic matter, enhancing infiltration and reducing surface runoff potential. Underlying geology is predominantly compacted, deeply weathered granite (80% of the area), with smaller portions of gneiss and dolomite. Fractured granite facilitates vertical and lateral subsurface flow, contributing to delayed groundwater responses. Slug tests estimated the saturated hydraulic conductivity of weathered granite to range from 5.2×10^{-3} m/day to 1.16 m/day.

2.2 Research hillslopes and instrumentation

Three research hillslopes (Hillslope 1, Hillslope 2, and Hillslope 3) were selected to investigate hydrological processes under varying geological and topographical conditions. Hillslope 1 (HS1)

6

features thick soils overlying fractured granite, Hillslope 2 (HS2) has a highly permeable fractured block layer, and Hillslope 3 (HS3) consists of shallow soils over weakly weathered bedrock.

To capture spatial variability, SWC probes and boreholes were installed along hilltops, mid-slopes, and foot slopes. Groundwater boreholes, ranging from 5 to 26 m deep, were equipped with HOBO capacitance water level loggers to record GWLs (Fig. 1).2.3 Meteorological and streamflow data collection

Meteorological data spanning 2013–2023 were collected from four GRWS100 automatic weather stations (WS700, WS900, WS1000, and WS1100), positioned at elevations of 700, 900, 1000, and 1100 m, respectively. Rainfall was recorded at 10-minute intervals using six tipping-bucket rain gauges near the weather stations, and the data were averaged for analysis.

Streamflow was measured at the catchment outlet using a Parshall flume, with water levels logged every 5 minutes since 2014. Data from some events were excluded due to sensor malfunctions or poor data quality, including key rainfall events in 2018 and 2019. Despite these exclusions, 95 rainfall-runoff events were analyzed, offering robust data for investigating bimodal stormflow characteristics.

2.4 Soil water content and groundwater level monitoring

Volumetric SWC was monitored at eight sites using CS616 time-domain reflectometry (TDR) probes installed at 10 cm intervals from the surface to 80 cm depth. Five profiles were located along HS1, and three were near WS1000. Measurements were recorded every 10 minutes, and the arithmetic mean of SWC values was used for analysis.

GWLs (below the ground surface, hereinafter referred to as bgs) were observed in six boreholes distributed across the hillslopes. HOBO capacitance water level loggers recorded hourly data. To facilitate comparisons, GWLs were normalized using the method described by Detty and McGuire (2010). This normalization, expressed as the GWL index (I_G), standardizes GWLs across wells with varying ranges.

158   Groundwater levels were normalized following the method described by Detty and McGuire

159   (2010). For each well and event, the median height of the water table above the lowest recordable

160   depth of the instrument was calculated and normalized to the total observed range, where 0 represents

161   the minimum height and 1 represents the maximum height. This normalized value was referred to as

162   the groundwater index (I_G). We used I_G to facilitate comparisons across wells with different absolute

163   GWL ranges and to represent the overall GWL dynamics in the watershed.

164   Streamflow and SWC data were aggregated to hourly intervals for alignment with GWL data.

165   Preliminary analysis confirmed that the delayed second streamflow peak had response times

166   exceeding the hourly scale, rendering this aggregation sufficient for the study's purposes.

2.5 Rainfall-runoff event identification and hydrograph analysis

168   Rainfall events were identified using an intensity-based automatic algorithm described by Tian

169   et al. (2012) that defines event with rainfall intensity >0.1 mm/h and a minimum separation of six

170   hours between events. Events with cumulative rainfall exceeding 5 mm were analyzed.

171   Bimodal rainfall-runoff events were manually identified based on two criteria: (1) the presence

172   of a secondary, arch-shaped runoff peak occurring after rainfall cessation or during minimal

173   intermittent rainfall, and (2) A distinct separation between the direct (sharp) and delayed (broad) peaks.

174   More details of the classification are described in Cui et al. (2024, HESS).

175   The combination of automatic event delineation and manual identification ensured the accurate

176   selection of 14 rainfall-runoff events with well-defined delayed peaks for subsequent analysis.

177   Streamflow was separated into storm runoff and baseflow using the HYSEP program with the

178   constant slope method (Hewlett and Hibbert, 1967; Sloto & Crouse, 1996), supplemented by manual

179   adjustments for complex hydrographs. Event stormflow volumes were calculated as total discharge

180   minus baseflow.

181   Streamflow was separated into storm runoff and baseflow using the HYSEP computer program

182   with the constant slope method, supplemented by manual adjustments for complex hydrographs.

183   Throughout the manuscript, stormflow refers to the total discharge, and event stormflow volumes

184   were calculated as total discharge minus baseflow, which are expressed in q_s.

185   **2.6 Hydrological connectivity analysis**

186   Hydrological connectivity among streamflow, SWC, and GWL was analyzed to examine the

187   interplay of subsurface flow pathways. Rainfall-runoff events were analyzed based on their total

188   rainfall (>5 mm) and corresponding streamflow peaks. As illustrated in Fig. 2, The peak rainfall

189   intensity (R_p) was determined based on the maximum 1-hour rainfall intensity, with the time of

190   occurrence recorded as TP_p. Metrics such as initial streamflow (Q_0) and peak streamflow (Q_p) were

191   determined alongside their respective timings (TQ_0 and TQ_p).

192   Similar metrics were calculated for SWC and GWL, including initial values (SWC_0 and I_{G0}) and

193   peak values (SWC_p and I_{Gp}), with corresponding times of occurrence (TS_0, TI_{G0}, TS_p and TI_{Gp}). These

194   metrics allowed for a comprehensive evaluation of the soil water-groundwater-streamflow response

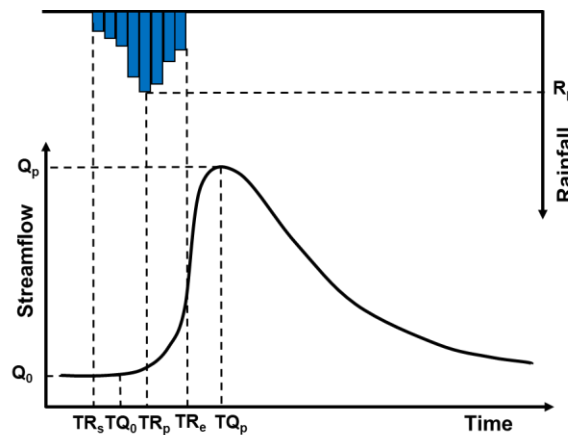195   relationship across 95 distinct rainfall-runoff events.

196

197   **Figure 2.** Definition sketch for analysis of rainfall event.

198   **3. Results**

199   **3.1 Hillslope-scale dynamics of SWC and GWL during rainfall-runoff events**

200   The temporal evolution of SWC and GWL was analyzed across 95 rainfall-runoff events to

9

understand their dynamic interaction. Our analysis revealed a clear relationship between SWC and GWL dynamics, with SWC initially increasing rapidly during rainfall, followed by a stabilization or decline once a threshold was reached. In contrast, GWL showed a more delayed response (Fig. 3). Three distinct patterns of SWC and GWL interaction were identified.

Figure 3 illustrates the dynamics of SWC and GWL during three representative events. These events were selected to demonstrate the variability in SWC and GWL patterns identified across the 95 rainfall-runoff events. The selected events all occurred within the same year to minimize inter-annual variability and ensure comparability. Red circles indicate rainfall periods, while black circles represent post-rainfall periods. In dry conditions, despite 66.6 mm of rainfall, SWC remained relatively low (<0.20), with a gradual increase during rainfall followed by stabilization after rainfall ceased. GWL showed minimal response. (Fig. 3a).
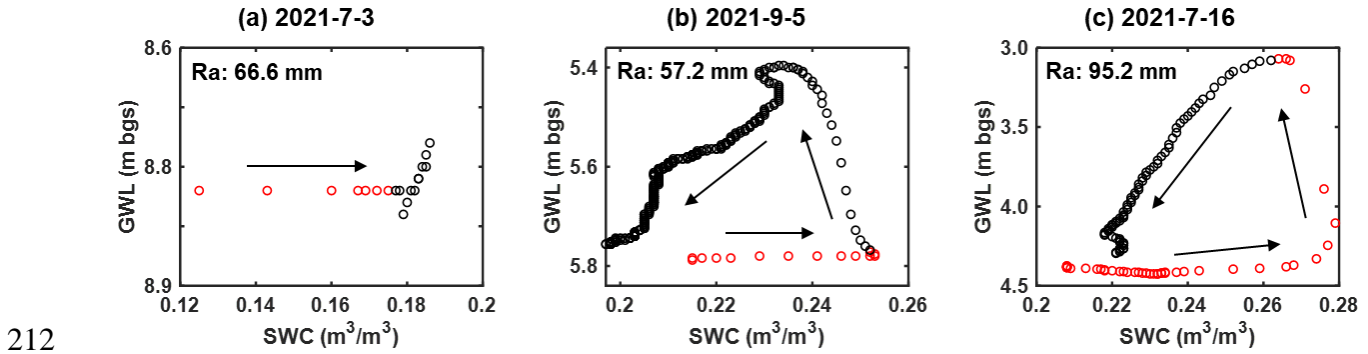
Figure 3. Three typical SWC-GWL dynamics patterns during rainfall-runoff events. Ra is rainfall amount. Arrows indicate the temporal evolution of the events. Red circles indicate periods of rainfall, while black circles denote post-rainfall periods.

In events with wet conditions, both SWC and GWL showed significant increases. However, the timing of GWL rise varied: in some cases, GWL rose after the cessation of rainfall, while in other cases, it began rising before the rainfall ended. The primary distinction between these patterns lies in the timing of the GWL rise: in Fig. 3b (57.2 mm rainfall), GWL began to rise after the rainfall ended, whereas in Fig.3c (95.2 mm rainfall), GWL started to rise noticeably before the end of the rainfall.

In the scenario represented by Fig. 3b, SWC increased significantly, surpassing 0.20, while GWL showed a delayed rise after the rainfall ceased. The counterclockwise hysteresis was observed as

10

223   SWC continued to increase while GWL remained largely unchanged during rainfall. Fig. 3c, which

224   typically represents intense storm events, showed a sharp increase in both SWC and GWL, with SWC

225   exceeding 0.25. GWL began to rise before the rainfall ended, reaching a peak as rainfall continued,

226   and both variables showed a substantial decline after rainfall ceased. These representative events

227   highlight the variability in the SWC-GWL relationship, with timing differences in the rise of GWL

228   and distinct hysteresis patterns during moderate and extreme events.

229   We further quantified the frequency distribution of SWC and GWL increases or decreases across

230   the 95 rainfall-runoff events (Fig. 4). Notably, in 49 events, SWC increased, while GWL increased in

231   43 events. In contrast, SWC declined in 26 events and GWL declined in 15 events. Importantly, 15

232   events showed a simultaneous decline in both SWC and GWL, which were associated with delayed

233   stormflow and larger stormflow volumes. One such event, on August 15, 2021, exhibited fluctuating

234   SWC and GWL values throughout the rainfall event due to the more dispersed rainfall distribution.

235   As a result, our subsequent analysis primarily focused on the remaining 14 events with well-defined
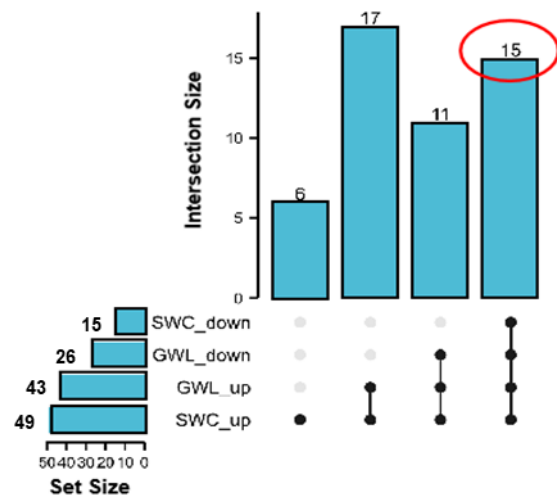
236   response characteristics.

237

238   **Figure 4**. Upset plot of the response characteristics of SWC and GWL during rainfall-runoff events.

239   **3.2 SWC dynamics across rainfall-runoff events**

240   Figure 5 presents the SWC dynamics observed during 14 distinct rainfall-runoff events, each

241 characterized by minimal or no intermittent rainfall during the recession period. To facilitate a clear

242 comparison of SWC changes across events, the peak of each event was aligned with a horizontal axis

243 value of 0.

244 During the initial rainfall phase, SWC increased rapidly, reaching a peak value. As the rainfall

245 ceased, SWC began to decline, though at a slower rate, eventually stabilizing at a specific value. To

246 quantify the threshold at which SWC stabilizes, we conducted a statistical analysis of the stable SWC

247 during these events. The stable phase was defined as the period following the recession phase when

248 SWC exhibited minimal variation before subsequent rainfall. The statistical analysis of the stable

249 SWC revealed a mean value of 0.1974, with a standard deviation of 0.0158 and a 95% confidence

250 interval of [0.1945, 0.2003]. These results validate the visually observed threshold of 0.20 for SWC

251 stabilization. The general pattern of SWC variation is schematically illustrated in Fig. 6.
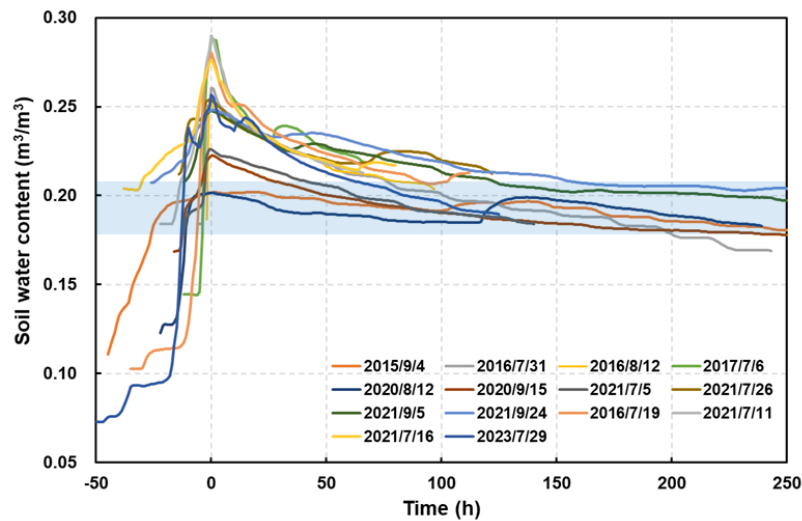
252

253 **Figure 5.** SWC dynamics during different storm events.

254 The SWC response to rainfall is rapid. Upon rainfall onset, SWC increased sharply. Once the

255 rainfall ceased, the subsequent behavior of SWC depends on whether the peak value exceeds the 0.20

256 threshold. If SWC remains below or at 0.20, it either stabilizes or declines slowly. However, when

257 SWC exceeds 0.20, it decreased rapidly before stabilizing around the 0.20 threshold. The magnitude

258 of the peak above 0.20 influences the speed of the subsequent decline in SWC: the greater the peak,
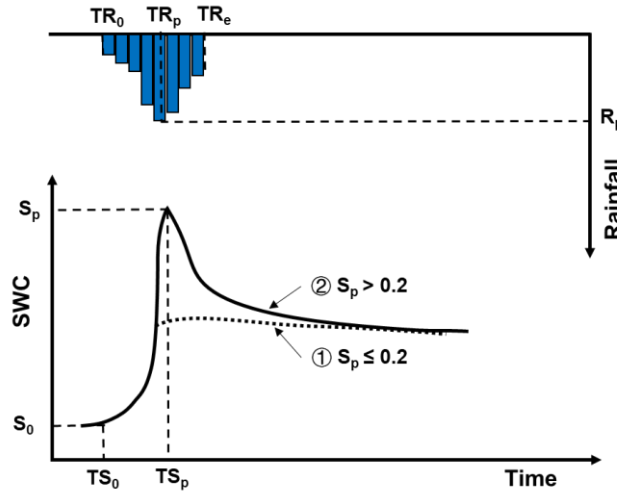
259 the faster the decline.

Figure 6. Schematic diagram of SWC response during storm events. S_p is the maximum SWC value.

3.3 GWL dynamics and response types

This section examines GWL dynamics during 14 selected rainfall-runoff events, chosen for their clear and consistent GWL and SWC patterns. These events facilitate a detailed investigation into groundwater response to storm events. Two distinct GWL response types—quick and slow—were identified and are conceptually illustrated in Fig. 7. It is important to note that Fig. 7 is a schematic representation, not based on specific rainfall-runoff events, and does not include rainfall depth data.
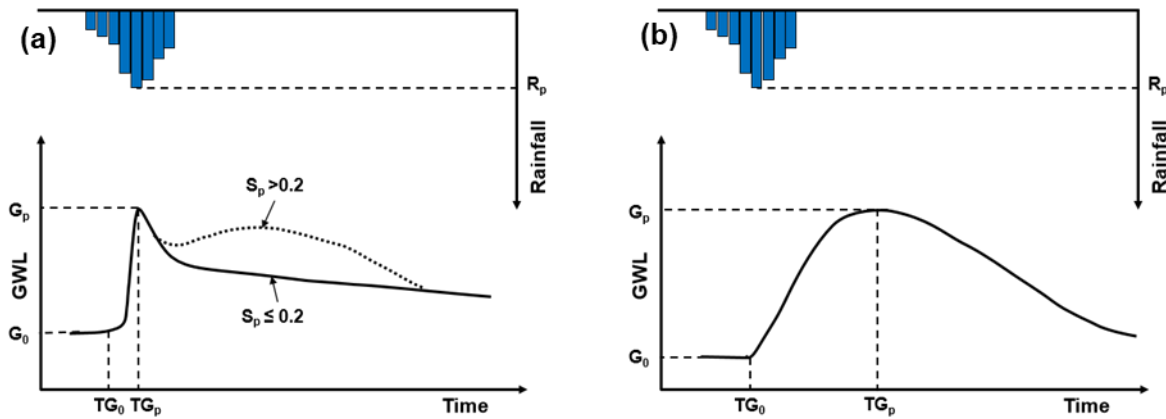

Figure 7. Schematic diagram of GWL response during storm events. G_0 and G_p represent the initial and maximum values of GWL, respectively. S_p denotes the maximum SWC value.

In events exhibiting a quick response, the GWL rises rapidly, closely aligning with the SWC

peak. The GWL response typically lags behind the SWC peak by 0 to 6 hours (Fig. 7a). For events where SWC exceeds 0.20 (and particularly when it surpasses 0.24), the GWL often shows a secondary rise following the initial peak, as indicated by the dotted line in Fig. 7a. Conversely, the slow response occurs when SWC declines sharply after reaching its peak, resulting in a delayed rise in GWL (Fig. 7b).

An analysis of GWL responses across various hillslopes revealed spatial variability. For instance, the GWL at HS2 (well W21-23) exhibited a quick response (Fig. 7a), whereas GWLs at HS1 (W13) and HS3 (W31 and W32) displayed slow response characteristics (Fig. 7b). These findings suggest that the GWL dynamics are influenced not only by SWC but also by the underlying geological structure of each hillslope.

At the watershed scale, GWL response to storm events demonstrated considerable spatial variability. I_G, represents the average normalized GWL across multiple wells, was used to capture an integrated view. Analysis revealed that I_G often exhibited two distinct peaks during storm events. Among the 14 events analyzed, 9 events displayed dual I_G peaks, coinciding with the two peaks in streamflow. However, at the individual well level, only W13 (HS1) and W23 (HS2) exhibited dual GWL peaks. Specifically, W13 showed two peaks during one event, while W23 exhibited two peaks during five events. The remaining wells displayed only a single peak across all events analyzed (see Table 1).

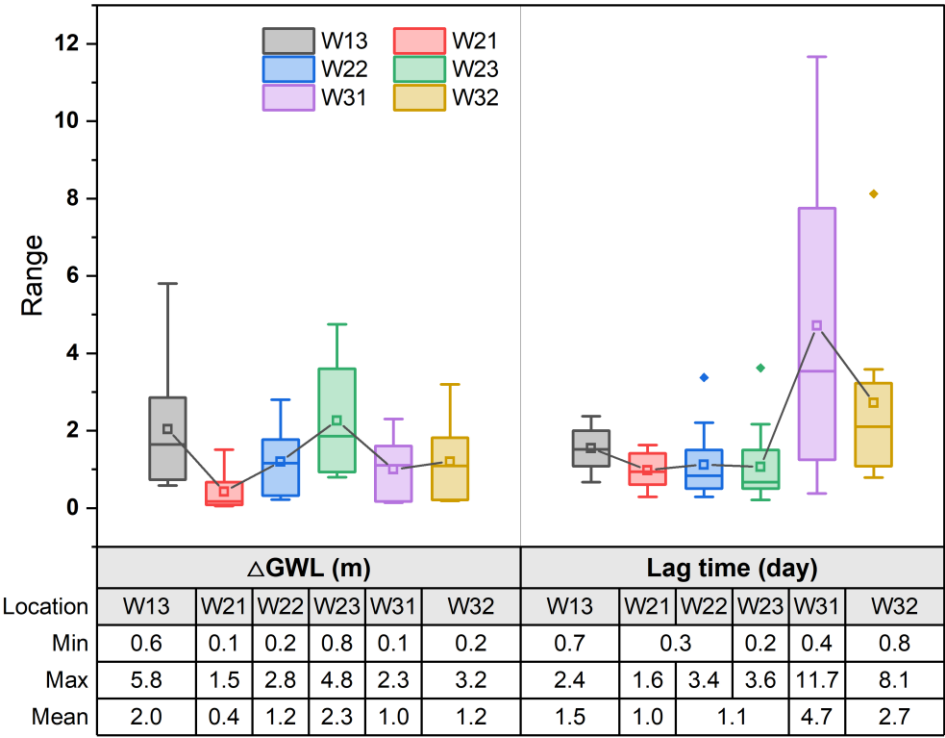**Table 1.** Statistical results of response characterization of streamflow, I_G and groundwater levels.

	Streamflow	I_G	HS1	HS2			HS3	
			W13	W21	W22	W23	W31	W32
Total number of events	14	14	14	8	14	14	9	9
Number of events with two peaks	9	9	1	0	0	5	0	0

3.4 GWL responses across hillslope positions

Further examination of GWL responses across various locations is presented in Fig. 8, which

shows the magnitude of GWL increases and their lag times relative to rainfall onset. While variations in GWL were observed among the monitoring wells, the differences in GWL increments were generally modest, with mean increases ranging from 1 to 2 meters. Notably, smaller GWL changes were recorded at the foot of the hillslope (e.g., W21 and W31). Within the same hillslope, GWL increments tended to increase progressively from the foot to the top, as seen in HS2 (W21-W23) and HS3 (W31 and W32).

Location	ΔGWL (m)						Lag time (day)					
	W13	W21	W22	W23	W31	W32	W13	W21	W22	W23	W31	W32
Min	0.6	0.1	0.2	0.8	0.1	0.2	0.7	0.3		0.2	0.4	0.8
Max	5.8	1.5	2.8	4.8	2.3	3.2	2.4	1.6	3.4	3.6	11.7	8.1
Mean	2.0	0.4	1.2	2.3	1.0	1.2	1.5	1.0	1.1		4.7	2.7

Figure 8. GWL increments (ΔGWL) and lag time of peak GWL relative to rainfall onset at different locations.

In contrast, the lag times for maximum GWL exhibited greater variation across locations. For instance, at HS3, lag times ranged from 0.4 to 11.7 days at W31 and from 0.8 to 8.1 days at W32, significantly longer than those at HS1 (0.7 to 2.4 days) and HS2 (0.2 to 3.6 days). Interestingly, within a single hillslope, no consistent relationship was found between the lag time of maximum GWL and its distance from the foot of the hillslope.

To further investigate these dynamics, the relationship between GWL increments and SWC was analyzed across 14 storm events (Fig. 9). The analysis focused on six observation wells (W13, W21–

W23, W31, and W32) located on three hillslopes (see Fig. 1 for well locations). The variability in GWL response types—quick versus slow—was attributed to spatial differences in SWC thresholds and hillslope geological structures.
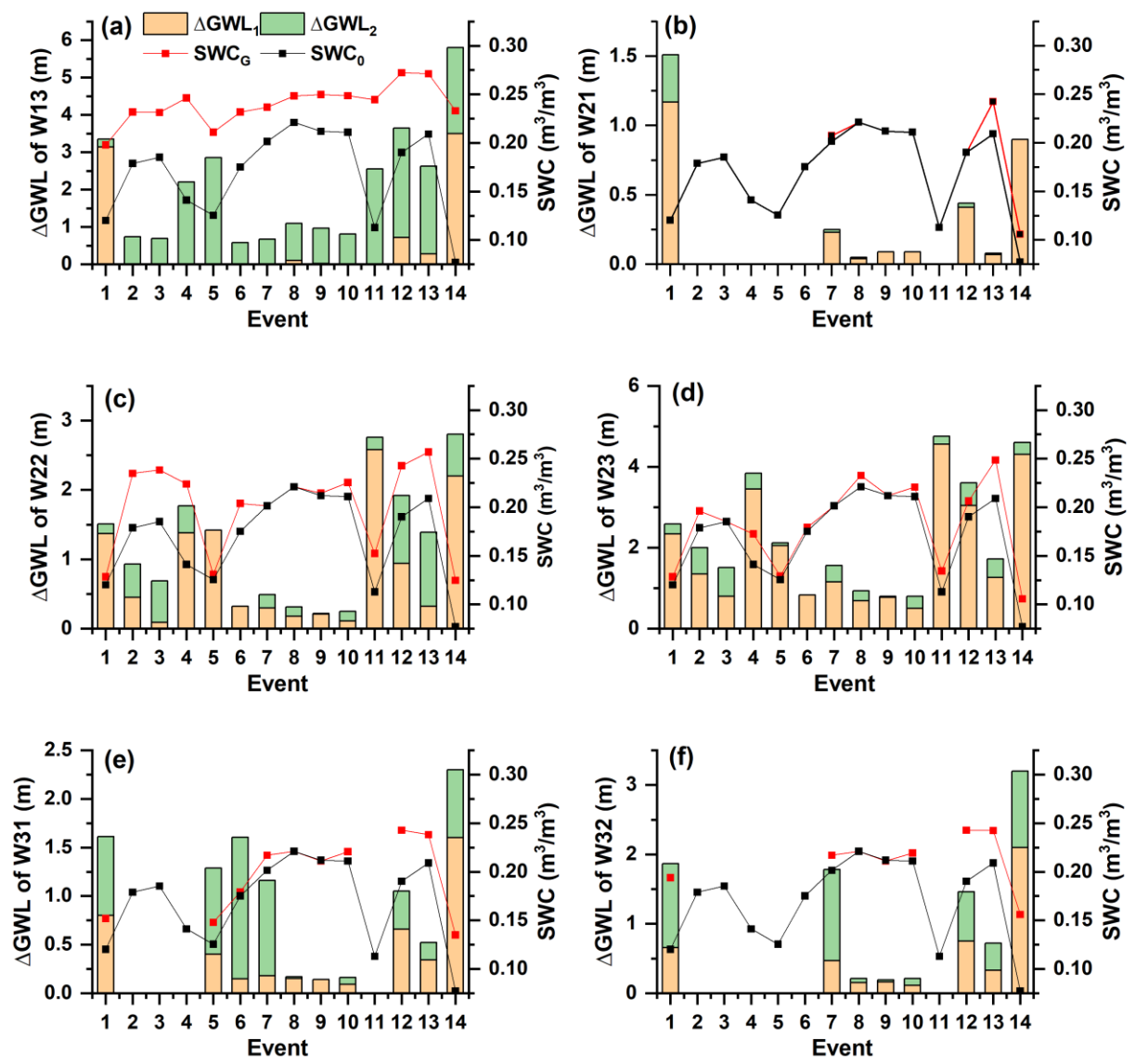

Figure 9. GWL increments (ΔGWL) across various locations during 14 storm events, along with initial SWC (SWC_0) and SWC at the onset of GWL rise (SWC_G). The orange bars represent ΔGWL during the SWC increase phase, while the green bars represent ΔGWL during the SWC decline phase. The red and black lines denote SWC_G and SWC_0, respectively.

In Fig. 9, the orange bars represent GWL increments during the SWC increase phase (up to its peak), while the green bars indicate GWL increments during the SWC decline phase (from its peak

16

320 to when GWL reached its maximum. The black and red dotted lines mark the initial SWC (SWC_0)

321 and the SWC at the onset of GWL rise (SWC_G), respectively. Missing data for some locations are

322 indicated by the absence of bars in Figs. 9b, 9e, and 9f.

323   The analysis revealed that the magnitude of the SWC increase following rainfall onset is a key

324 determinant of delayed GWL responses. Specifically, a greater difference between SWC_G and SWC_0

325 corresponded to an onset of GWL rise begins. Conversely, when SWC_G and SWC_0 are similar, GWL

326 rose almost simultaneously with the SWC increase.

327   At HS1 (W13), GWL began to rise only after SWC exceeded 0.20. Most of the GWL increase

328 occurred during the SWC decline phase, suggesting that soil wetness exerts a threshold effect on

329 GWL dynamics. This delayed response aligns with the slow response type. At HS2 (W21-23), GWL

330 responses were more immediate, with GWL increases closely following SWC rises. SWC_G values at

331 these locations ranged widely (0.13-0.26) but were generally close to SWC_0, indicating that GWL

332 responses at HS2 are less dependent on SWC thresholds and exhibit a quick response type.
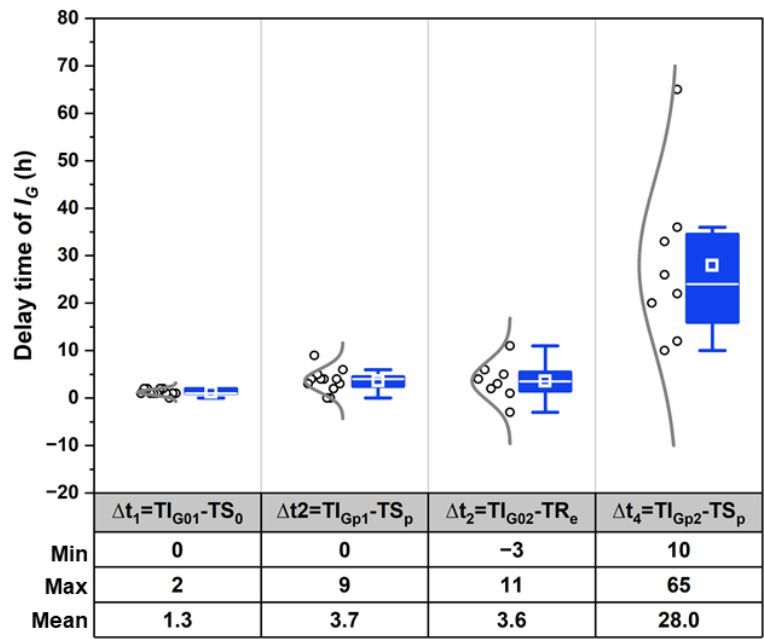
333   HS3 demonstrated both quick and slow GWL responses. Initial rises occurred soon after the

334 SWC increase, but the majority of GWL increments took place during the prolonged SWC decline

335 phase following its peak. This pattern suggests a more complex interaction of immediate and delayed

336 factors influencing GWL dynamics at HS3.

337   These findings highlight a strong relationship between the emergence of quick and slow GWL

338 response types and SWC dynamics. In quick response types, GWL increments occur primarily during

339 the SWC increase phase, resulting in a steep response curve. In slow responses, GWL increments

340 predominantly occur during the SWC decline phase, producing an arch-shaped response curve. These

341 distinctions underscore the pivotal role of SWC dynamics in regulating the timing and magnitude of

342 GWL responses across different hillslopes.

343 **3.5 Characterization of groundwater response at the watershed scale**

344   Figure 10 illustrates the timing of I_G peaks relative to SWC response. The first I_G peak occurred

rapidly following rainfall, initiating 0-2 h after the SWC began to rise and reaching its peak occurring
0-9 h later (mean: 3.7 h) after SWC reached its maximum. In contrast, the second I_G peak typically
occurred post-rainfall, lagging behind the SWC peak by 10-65 h (mean: 28 h). These patterns align
with the quick and slow GWL response types identified in section 3.2. The occurrence of dual I_G
peaks can be attributed to the superimposition of groundwater contributions from different hillslopes
with differing response rates. The first (quick) GWL response is tightly coupled to rainfall onset and
SWC increases, while the second (slow) GWL response reflects gradual infiltration and groundwater
recharge occurring over a broader timescale.

	$\Delta t_1 = TI_{G01} - TS_0$	$\Delta t2 = TI_{Gp1} - TS_p$	$\Delta t_2 = TI_{G02} - TR_e$	$\Delta t_4 = TI_{Gp2} - TS_p$
Min	0	0	−3	10
Max	2	9	11	65
Mean	1.3	3.7	3.6	28.0

Figure 10. Delay time of I_G peaks relative to peak SWC. TI_{G01} and TI_{G02} represent the onset times
of the first and second peaks of I_G, respectively. TS_0 and TS_p indicate the time when SWC started to
increase and peaked, respectively. TI_{Gp1} and TI_{Gp2} represent the time when I_G started to increase and
peaked, respectively. TR_e indicates the end of rainfall.

The growth rates of I_G towards the two peaks were also quantified (Fig. 11). A notable disparity
was observed between the growth rates of the first (r_1) and second (r_2) I_G peaks. The first I_G peak
exhibited a markedly faster rates (0.03 to 0.98/day, mean: 0.38/day) compared to the second peak
(0.01 to 0.31/day, mean: 0.07/day). These differences reflect the contrasting dynamics of quick and
slow GWL responses across hillslopes. In events featuring dual I_G peaks, the maximum I_G was

typically observed at the second peak. However, in events with higher GWLs (indicating lower I_G), the disparity between the growth rates diminished, making the two peaks harder to distinguish (e.g., Events 9 and 10). In Events 11-14, where GWLs were significantly higher, only a single I_G peak was observed.
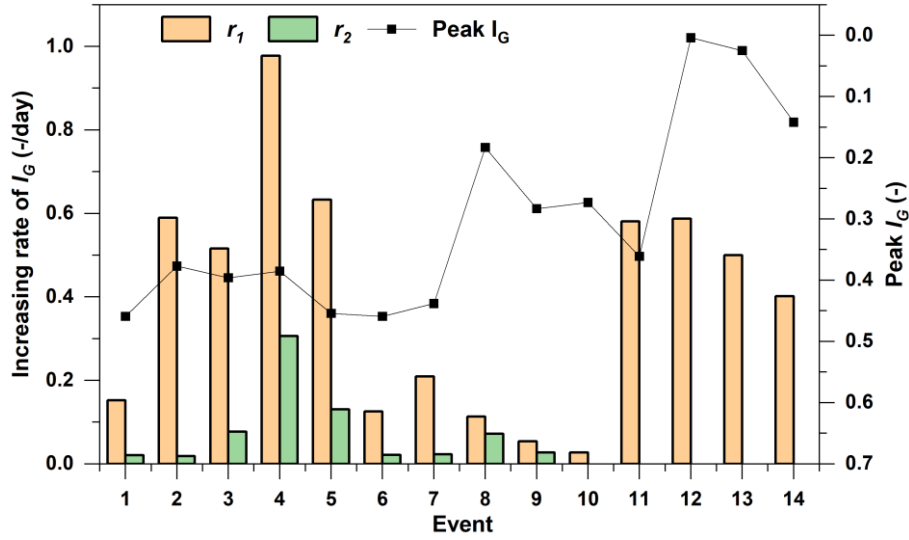
Figure 11. Growth rates of I_G and the maximum I_G value across storm events. r_1 and r_2 denote the ascent rates during the first and second peaks, respectively.

The contrasting dynamics of the two IG peaks highlight their distinct formation mechanisms. The first I_G peak, occurring during rainfall, is closely associated with the rapid rise in SWC. Conversely, the second I_G peak emerges post-rainfall, coinciding with soil draining and groundwater recharge processes. As reported by Dang et al. (2023), rainfall induces pressure waves that rapidly expel soil water from the lower soil column, while infiltrated rainwater migrates downwards at slower pace. pressure-driven displacement generates a near-instantaneous GWL response during the initial phase of rainfall.

We hypothesize that the rapid I_G peak is linked to kinematic wave triggered by increased SWC, which displaces pre-existing "old" soil water and groundwater, leading to a synchronized GWL rise (e.g., Anderson and Burt, 1978). Despite the slow percolation of water through soil and bedrock, the theoretical celerity of this kinematic response is near-instantaneous, accounting for the rapid GWL rise. Furthermore, drilling data suggest that the presence of faults in the bedrock of HS2, potentially

382 facilitating faster groundwater response on this hillslope compared to others.

383 The second, slow I_G peak is likely driven by the gradual infiltration of rainwater into deeper soil
384 and bedrock layers, ultimately recharging the groundwater. This process is regulated by the soil's
385 water storage threshold. Before reaching this threshold, the soil retains all incoming rainfall. Once
386 exceeded, excess water drains rapidly into deeper layers, leading to a decline in SWC and a concurrent
387 rise in GWL due to groundwater recharge.

## 4. Discussion

4.1 Inter-hillslope GWL dynamics

390 GWL variations in lag times and response magnitudes across hillslopes can be attributed to
391 differences in geological conditions. HS1 and HS3 are primarily underlain by fully to strongly
392 weathered granite, with upper layers comprising significant soil-rock mixtures. These features lead
393 to relatively slower GWL responses, likely due to the limited permeability of the regolith and
394 underlying materials. In contrast, HS2 is characterized by a fractured rock layer at depths of 10-30
395 meters (see Fig. 1), which enhances subsurface flow and facilitates faster GWL responses. These
396 geological contrasts explain the observed differences in GWL response times among the hillslopes.

397 Among the three hillslopes, HS3 exhibited the slowest GWL responses, characterized by the
398 longest lag times. This distinct behavior makes HS3 a crucial reference for understanding inter-
399 hillslope variations in GWL dynamics. Previous study by Cui et al. (2024) highlighted that GWL
400 response times are closely linked to delayed stormflow timing, emphasizing the importance of
401 examining GWL dynamics. Comparing the GWL response times of HS1 and HS2 with those of HS3
402 provides insights into how geological structures and SWC thresholds influence delayed stormflow
403 generation.

404 Furthermore, the deeply weathered regolith and extensive fracturing in HS2 promote more rapid
405 stormflow generation, as water stored in the regolith layer contributes to streamflow over extended
406 periods. This finding aligns with previous studies (Kosugi et al., 2011; Padilla et al., 2015), which

407   demonstrated that geological features such as fracture density and weathering depth influence

408   subsurface flow paths and, ultimately, groundwater dynamics.

409   To deepen understanding of the inter-hillslope differences in GWL responses, we calculated the

410   lag times between rainfall onset and peak GWL responses for all observation wells on each hillslope,

411   incorporating spatial variability. Average lag times, denoted as t_{S1}, t_{S2} and t_{S3} for HS1, HS2, and HS3,

412   respectively, were used to calculate the time differences $\Delta t = t_{S1} - t_{S3}$ and $\Delta t = t_{S2} - t_{S3}$. These time

413   differences were then analyzed for their correlation with I_G, as illustrated in Fig. 12.

414
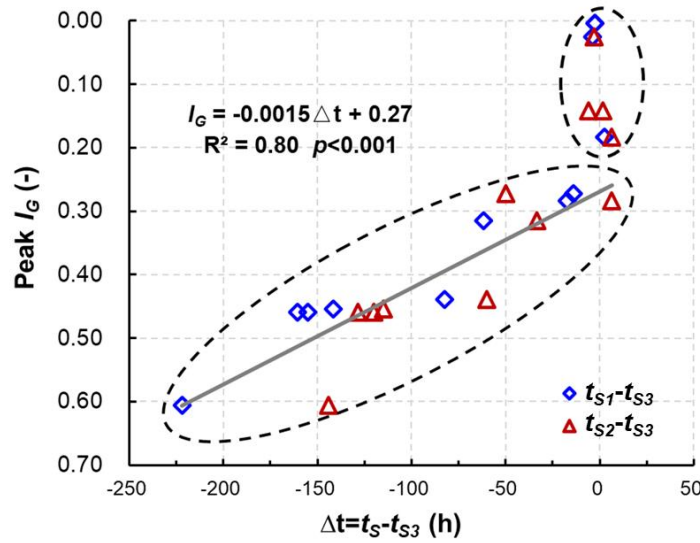
Figure 12. Correlation between peak I_G and the time differences from peak GWL responses on
HS1, and HS2 to HS3 ($\Delta t = t_S - t_{S3}$), where t_{S1}, t_{S2} and t_{S3} are the average lag times of peak GWLs on
HS1, HS2 and HS3, respectively.

418   In Fig. 12, blue diamonds represent $\Delta t = t_{S1} - t_{S3}$, while red triangles represent $\Delta t = t_{S2} - t_{S3}$. Both

419   pairs exhibit a significant negative correlation with peak I_G, described by the equation: $I_G = -$

420     $0.0015 \times \Delta t + 0.27$ ($R^2 = 0.80$, $p < 0.001$). These results indicate that higher I_G values correspond to

421   shorter inter-hillslope lag times, suggesting enhanced hydrological connectivity and transmissivity

422   feedback mechanisms, as described in previous studies (Kendall et al., 1999; Bishop et al., 2011).

423   As peak I_G approaches 0.30, Δt converges to near-zero with minimal fluctuations, particularly

424   during extreme storm events. This finding supports the results presented in Fig. 11, which demonstrate

425   that elevated GWLs synchronize GWL responses across the watershed. This synchronization reflects

426   a critical hydrological mechanism driven by transmissivity feedback, which amplifies groundwater

427   movement, reduces lag times, and enhances watershed-scale connectivity. This dynamic is consistent

428   with the work of Padilla et al. (2015), who reported that shorter lag times in bedrock aquifers with

429   high-transmissivity conduits, and Scaife et al. (2020), who noted that increased connectivity during

430   high GWL conditions reduces lag times and enhances watershed-scale hydrological responses.

431   Furthermore, although Fig. 12 labels the vertical axis as I_G to represent watershed-wide GWL

432   status, a similar pattern emerges when replacing I_G with site specific GWL values, though the GWL

433   thresholds may vary among observation sites. These observations reinforce the idea that watershed-

434   scale groundwater dynamics are influenced by the interplay between spatially variable geological

435   conditions and temporal variations in GWL.

436   **4.2   Delayed stormflow processes linked to GWL dynamics**

437   Previous studies have shown that streamflow in XEW frequently exhibits a bimodal hydrograph

438   during heavy rainfall, with delayed stormflow likely originating from shallow groundwater outflow

439   (Cui et al., 2024). Understanding the timing and lag between groundwater and streamflow responses

440   is crucial for identifying dominant runoff generation mechanisms (Beiter et al., 2020). Discrepancies

441   in these timings can indicate contributions from different water sources to the stream channel. Fig.

442   13 illustrates the relative timing of maximum I_G (I_{Gp}) and maximum SWC (SWC_p) for eight storm
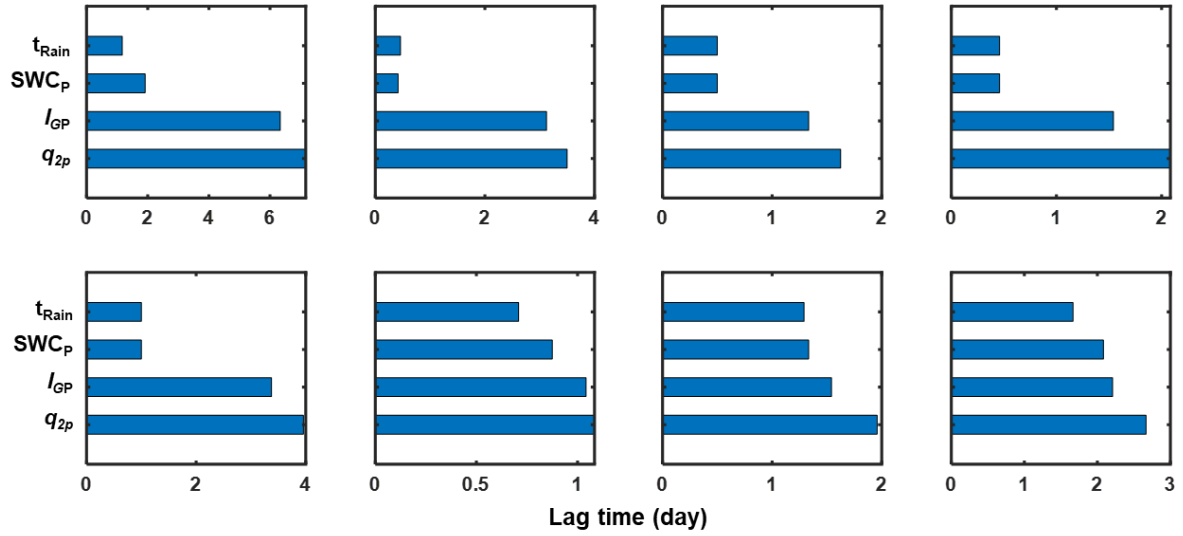
443   events, alongside rainfall duration.

Figure 13. Lag times of maximum SWC and GWL relative to rainfall onset. Each bar indicates the rise and peak times of the corresponding variable, with t_{Rain} indicating rainfall duration. SWC_{SP} and I_{GP} represent the maximum SWC and I_G, respectively, while q_{2p} denotes the delayed streamflow peak.

Rainfall durations for the analyzed events ranged from 0.46 to 1.67 days. SWC, I_G, and delayed stormflow (q_{2p}) followed a clear sequence in their peak timings relative to rainfall onset. SWC responded rapidly, with its peak occurring 0.4 to 2.1 days after rainfall began, usually coinciding with or slightly after rainfall cessation. In contrast, I_G continued to increase after the SWC peak and reached its maximum before the delayed stormflow peak (q_{2p}). While the lag times between SWC_p, I_{Gp}, and q_{2p} varied among events, the lag between I_{Gp} and q_{2p} remained relatively consistent.

This pattern aligns with findings from Haught and Meerveld (2011) and Rinderer et al. (2016), who suggest that when groundwater response precedes or synchronizes with streamflow, it indicates strong hillslope-stream connectivity, with groundwater serving as the primary driver of streamflow. Our results corroborate this view, showing that q_{2p} timing is predominantly governed by groundwater dynamics. This relationship is further validated by the strong linear correlation between the lag times of q_{2p} (t_{2p}) and I_{Gp} (t_{IGp}), as indicated by the regression equation $t_{2p} = 1.11 \times t_{IGp} + 0.17$, with a slope of 1.11, showing a high determination coefficient ($R^2 = 0.995$, $p < 0.01$). (Fig. 14).

Conversely, the correlation between t_{2p} and the lag time of SWC_p (t_{SWCp}) was weak ($R^2 = 0.029$,

463    $p = 0.688$), indicating that the timing of SWC_p has minimal influence on the delayed streamflow peak.

464   Additionally, the I_G pattern during the delayed stormflow period closely mirrored the shape of the

465   streamflow hydrograph (Fig. A1), reinforcing the dominant role of I_G plays in controlling delayed

466   stormflow.
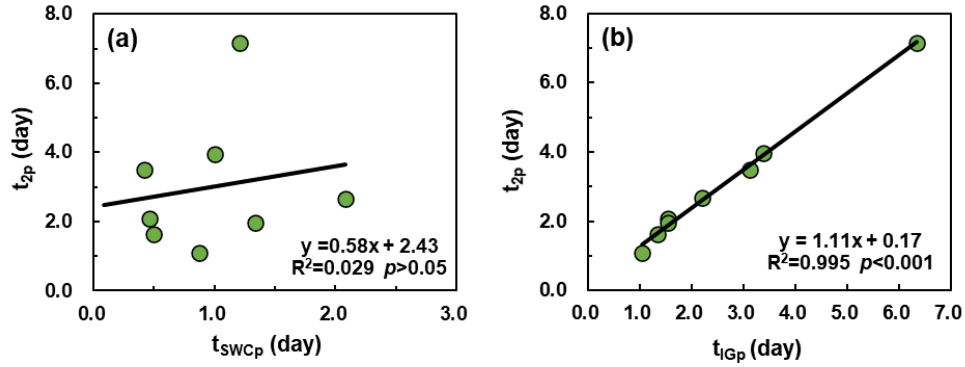
467

468   **Figure 14.** Lag times of maximum (a) SWC and (b) I_G relative to delayed streamflow peaks (t_{2p}).
469   t_{SWCp} and t_{IGp} denote the peak times of the SWC and I_G, respectively.

470   Further quantitative analysis revealed a strong exponential relationship between streamflow and

471   I_G during the delayed stormflow period (Fig. 15). In the non-rainfall phase of the eight bimodal events,

472   streamflow increased exponentially with GWL (IG_p), exhibiting a highly significant correlation ($p <$

473   0.001) and a determination coefficient of $R^2 = 0.90$. This exponential increase in streamflow is

474   attributed to the increase in lateral hydraulic conductivity as the water table approaches the surface.

475   Similar findings have been reported by Detty and McGuire (2010) and Kendall et al. (1999), where

476   groundwater outflow dominates during storm events.

477
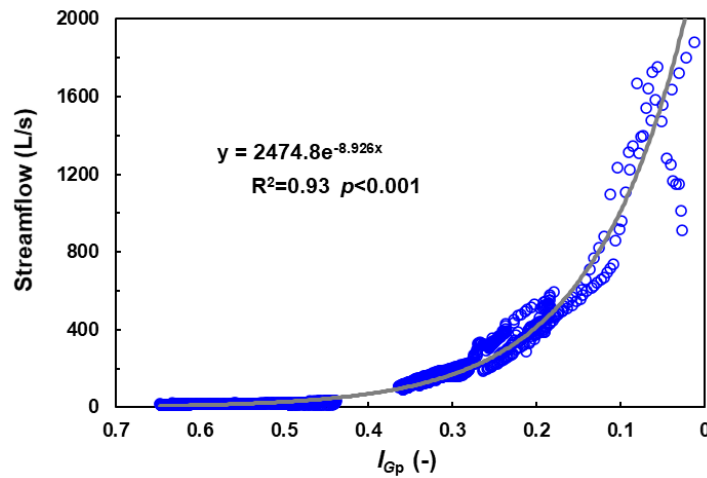
478   **Figure 15.** Correlation between I_G and streamflow during delayed stormflow periods.

479   At higher GWLs, the curve of GWL vs. streamflow begins to flatten, suggesting a feedback

480 mechanism. As the rising water table mobilizes shallow groundwater outflow, water is rapidly

481 transported to the stream via shallow flow paths. This process, often referred to as transmissivity

482 feedback, is consistent with Lundin's (1982) description of groundwater dynamics during delayed

483 stormflow periods.

484   **4.3   Delayed stormflow processes linked to GWL dynamics**

485   Understanding the critical thresholds that govern the movement of water within landscapes is

486 essential for accurately predicting delayed stormflow, as emphasized by McDonnell et al. (2021).

487 This study identified a strong Relationship between delayed stormflow and the gradual response of

488 GWL, primarily influenced by a sharp decline in SWC when it exceeds a critical threshold of 0.20.

489   To identify the threshold for delayed stormflow initiation in XEW, we analyzed 63 out of 95

490 rainfall-runoff events with complete streamflow data. The relationship between SWCp and q_s for

491 these events is illustrated in Fig. 16. A clear threshold behavior emerged: when SWC was below 0.20,

492 q_s remained minimal consistent with unimodal events. However, as SWC exceeded 0.20, a noticeable

493 increase in q_s was observed, signaling the onset of delayed stormflow in some events. Specifically,

494 when SWC surpassed 0.23, a pronounced surge in stormflow volume occurred, accompanied by the

495 emergence of a secondary stormflow peak in all events. These findings suggest that the critical

496 threshold for delayed stormflow initiation lies within the SWC range of 0.20 to 0.23.
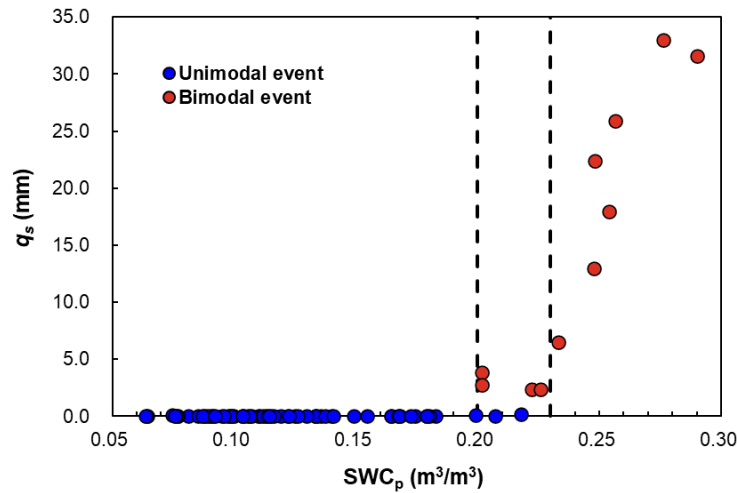
Figure 16. Relationship between maximum SWC (SWC_p) and event stormflow volume (q_s).

497

498

These results underscore the pivotal role of the surface soil layer's water deficit or water-holding capacity in triggering delayed stormflow. During rainfall events, the soil retains water until its water-holding capacity is exceeded. Once SWC surpasses the threshold of 0.20, the soil begins to release water more rapidly, initiating delayed stormflow. Additionally, during unimodal events, stormflow (q_s) remained consistently below 1 mm despite variations in SWC, indicating that stormflow in these cases arises mainly from direct rainfall interception by the channel rather than delayed soil water release.

While the depth and distribution of soil layers likely influence the watershed's overall water storage capacity, observed SWC data showed minimal spatial variability across locations within the watershed. This suggests that SWC can reliably represent the watershed's overall soil water storage capacity.

One limitation of this study lies in the indirect estimation of field capacity through observed SWC thresholds rather than direct measurement or modeling. Although this approach aligns with observed patterns and simplifies the analysis, it does not fully capture the spatial variability of field capacity or its dependence on soil depth. Future work should incorporate direct field capacity measurements or modeling to refine the relationship between SWC and delayed stormflow initiation, thereby improving the accuracy of threshold predictions.

4.4 Conceptual model of runoff generation in XEW

This section presents a conceptual model elucidating the runoff generation mechanisms in XEW, with a particular focus on the interplay between soil water storage and GWL dynamics. Soil water storage is identified as the critical factor driving the transition from initial to delayed runoff generation. Once the soil water deficit is replenished, the slowly rising GWL becomes the dominant control in the delayed stormflow process. Fig 17 illustrates the conceptual framework, which incorporates transmissivity feedback mechanisms to explain the formation of distinct hydrograph patterns.

1. Runoff generation under dry conditions (Fig. 17b):

In dry watershed conditions, characterized by low antecedent moisture and light rainfall, rainwater primarily infiltrates and is retained in the soil profiles. Streamflow during such events consists of two primary components: (1) a rapid yet modest streamflow peak driven by direct rainfall onto the channel and (2) a relatively stable baseflow originating from the gradual release of deep groundwater reservoirs.

Under these conditions, the baseflow reflects the slow release of groundwater stored in deeper aquifers, while the limited rainfall input is insufficient to trigger significant connectivity between hillslopes and the channel.

2. Delayed stormflow during moderate storms (Fig. 17c):

As rainfall intensity and duration increase, moderate storm events lead to the replenishment of soil water deficits, resulting in the exceedance of soil storage capacity. Initially, the response resembles that of dry conditions, with a rapid streamflow peak generated by direct channel rainfall. However, as rainfall continues, excess water infiltrates deeper, elevating the GWL and expanding the saturated zone.

This process enhances the hydraulic connectivity between the stream channel and adjacent hillslopes, facilitating the lateral transport of shallow groundwater to the channel. As the GWL intersects more conductive soil layers, a delayed stormflow peak is observed, typically occurring after

541 rainfall ceases. This secondary peak reflects the combined effects of deep infiltration, gradual GWL

542 rise, and increased transmissivity in the subsurface, which accelerates shallow groundwater

543 movement towards the channel.

3. Runoff generation during extreme storm events (Fig. 17d):

545 Extreme storm events, characterized by high rainfall intensity and large volumes, result in a

546 sharp and widespread rise in GWL across the entire watershed. During such events, the rapid

547 expansion of saturated areas and the increased hydraulic conductivity of the subsurface enable the

548 swift mobilization of shallow groundwater. This synchronous response generates a pronounced flood

549 peak within a short timeframe.

550 In the riparian zones, GWLs may rise into the soil profile or even reach the ground surface,

551 facilitating direct water flow into the channel via subsurface pathways. Observational data from

552 extreme events corroborate this mechanism, as significant increases in SWC are recorded in the

553 deeper soil layers of riparian zones after rainfall ends. This pattern suggests that groundwater from

554 adjacent hillslopes contributes to the replenishment of soil water in these zones, reinforcing lateral
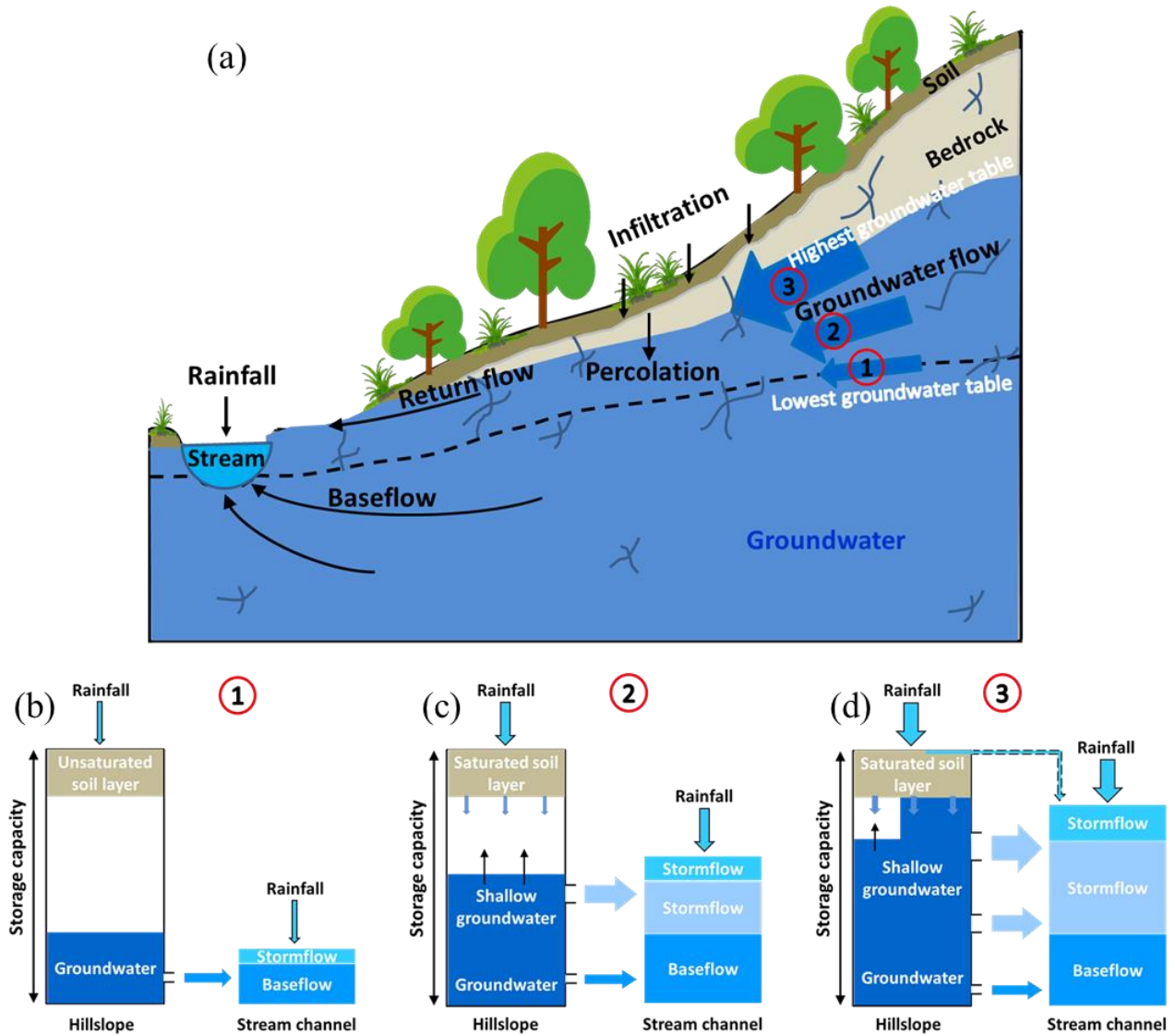
555 subsurface flow pathways.

Figure 17. Conceptual model illustrating stormflow generation associated with the transmissivity feedback.

The progression from the runoff generation under dry conditions (Fig. 17b) to moderate storm scenarios (Fig. 17c) and ultimately extreme events (Fig. 17d) reflects the progressive wetting-up of the watershed. Abrupt changes in stormflow volume and timing are initially governed by soil water storage thresholds and subsequently controlled by the hydraulic conductivity of the bedrock and micro-topography.

This conceptual model provides a quantitative framework for understanding how variations in hydrological conditions influence runoff generation processes in XEW. By integrating soil water

storage dynamics, GWL responses, and transmissivity feedback mechanisms, the model offers insights into the nonlinear behavior of runoff processes under different rainfall scenarios.

5. Conclusions

Building upon previous work that identified and characterized bimodal streamflow patterns in XEW, this study quantitatively analyzed SWC and GWL dynamics at the event scale to elucidate the mechanisms driving delayed stormflow generation. The findings reveal that when soil water storage surpasses its holding capacity, a secondary increase in streamflow is triggered. This secondary, or delayed, stormflow is primarily governed by GWL dynamics, which dictate both the magnitude of the delayed response and the lag time to its peak.

During rainfall events, SWC responds rapidly, increasing until the soil's water storage capacity is reached or exceeded. If the stored water remains within this capacity, SWC stabilizes or decreases gradually following the cessation of rainfall, eventually leveling off near the field capacity. The rate of this decrease is closely linked to the extent of SWC exceeding the field capacity. When SWC begins to decline, excess rainwater percolates deeper into the soil, raising the GWL. Once GWL begins to rise, it becomes the dominant driver of the delayed stormflow process.

As GWL rises, hydraulic conductivity increases, facilitating enhanced groundwater flux from hillslopes to the stream channel. This process expands the effective connectivity between the channel and adjacent hillslopes. At specific high GWL thresholds, the synchronization of GWL responses across multiple hillslopes significantly amplifies stormflow volume. This synchronized response shortens the lag time and increases the volume of delayed stormflow, often merging the delayed peak with the direct stormflow peak.

These findings offer critical insights into the nonlinear processes governing stormflow generation and the formation of bimodal hydrographs. By elucidating the mechanisms underpinning these dynamics, the study advances hydrological theory and provides actionable knowledge for improving flood modeling and prediction.

Data availability

The data supporting this study are available on the Zenodo website at https://doi.org/10.5281/zenodo.12581739.

Author contribution

ZC contributed the conceptualization, formal analysis, investigation and writing; FT contributed the conceptualization, formal analysis and revision.

Competing interests

Fuqiang Tian is a member of the editorial board of Hydrology and Earth System Sciences.

Acknowledgements

5. References

Ali, G., Oswald, C. J., Spence, C., Cammeraat, E. L., McGuire, K. J., Meixner, T., and Reaney, S. M.: Towards a unified threshold-based hydrological theory: necessary components and recurring challenges, Hydrol. Process., 27, 313–318, https://doi.org/10.1002/hyp.9560, 2013.

Anderson, M. G., and Burt, T. R.: The role of topography in controlling throughflow generation, Earth Surf. Process., 3, 331–334, https://doi.org/10.1002/esp.3290030402, 1978.

Beiter, D., Weiler, M., and Blume, T.: Characterising hillslope–stream connectivity with a joint event analysis of stream and groundwater levels, Hydrol. Earth Syst. Sci., 24, 5713-5744, https://doi.org/10.5194/hess-24-5713-2020, 2020.

Bishop, K., Seibert, J., Nyberg, L., and Rodhe, A.: Water storage in a till catchment. II: Implications of transmissivity feedback for flow paths and turnover times, Hydrol. Process., 25, 3950-3959, https://doi.org/10.1002/hyp.8355, 2011.

Cain, M. R., Woo, D. K., Kumar, P., Keefer, L., and Ward, A. S.: Antecedent conditions control thresholds of tile-runoff generation and nitrogen export in intensively managed landscapes, Water Resour. Res., 58,

616   e2021WR030507, https://doi.org/10.1029/2021WR030507, 2022.

617   Cui, Z., Tian, F., Zhao, Z., Xu, Z., Duan, Y., Wen, J., and Khan, M. Y. A.: Bimodal Hydrographs in Semi-humid

618   Forested Watershed: Characteristics and Occurrence Conditions, Hydrol. Earth Syst. Sci. Discuss.,

619   https://doi.org/10.5194/hess-2024-36, 2024.

620   Dang, L., Xie, Y. Q., Wang, C., Chang, Y., Zeng, X. K., and Wu, J. C.: Precipitation-induced Pressure Wave

621   Propagation in Unsaturated Zone and Its Effect on Rapid Groundwater Discharge, Geol. J. China Univ., 29,

622   580-589, https://doi.org/10.16108/j.issn1006-7493.2021104, 2023.

623   Detty, J. M., and McGuire, K. J.: Threshold changes in storm runoff generation at a till-mantled headwater catchment,

624   Water Resour. Res., 46, W07525, https://doi.org/10.1029/2009WR008102, 2010.

625   Farrick, K. K., and Branfireun, B. A.: Soil water storage, rainfall and runoff relationships in a tropical dry forest

626   catchment, Water Resour. Res., 50, 9236-9250, https://doi.org/10.1002/2014WR016045, 2014.

627   Fu, C., Chen, J., Jiang, H., and Dong, L.: Threshold behavior in a fissured granitic catchment in southern China: 1.

628   Analysis of field monitoring results, Water Resour. Res., 49, 2519-2535, https://doi.org/10.1002/wrcr.20193,

629   2013.

630   Graeff, T., Zehe, E., Reusser, D., Lück, E., Schröder, B., Wenk, G., John, H., and Bronstert, A.: Process identification

631   through rejection of model structures in a mid-mountainous rural catchment: observations of rainfall-runoff

632   response, geophysical conditions and model inter-comparison, Hydrol. Process., 23, 702–718,

633   https://doi.org/10.1002/hyp.7171, 2009.

634   Graham, C. B., and McDonnell, J. J.: Hillslope threshold response to rainfall: (2) development and use of a

635   macroscale model, J. Hydrol., 393, 77–93, https://doi.org/10.1016/j.jhydrol.2010.03.008, 2010.

636   Graham, C. B., Woods, R. A., and McDonnell, J. J.: Hillslope threshold response to rainfall: (1) A field based

637   forensic approach, J. Hydrol., 393, 65–76, https://doi.org/10.1016/j.jhydrol.2009.12.015, 2010.

638   Haga, H., Matsumoto, Y., Matsutani, J., Fujita, M., Nishida, K., and Sakamoto, Y.: Flow paths, rainfall properties,

639   and antecedent soil moisture controlling lags to peak discharge in a granitic unchanneled catchment, Water

640   Resour. Res., 41, W2179–W2187, https://doi.org/10.1029/2005wr004236, 2005.

641   Haught, D. R. W. and Meerveld, H. J.: Spatial variation in transient water table responses: differences between an

642   upper and lower hillslope zone, Hydrol. Process., 25, 3866-3877, https://doi.org/10.1002/hyp.8354, 2011.

643   Hewlett, J. D., and Hibbert, A. R.: Factors affecting the response of small watersheds to precipitation in humid areas,

644   in: Forest Hydrology, edited by: Sopper, W. E. and Lull, H. W., Pergamon Press, Oxford, 275–290, 1967.

645   Jin, Z., Guo, L., Yu, Y., Luo, D., Fan, B., and Chu, G.: Storm runoff generation in headwater catchments on the

646   Chinese Loess Plateau after long-term vegetation rehabilitation, Sci. Total Environ., 748, 141375,

647   https://doi.org/10.1016/j.scitotenv.2020.141375, 2020.

648   Kendall, K. A., Shanley, J. B., and McDonnell, J. J.: A hydrometric and geochemical approach to test the

649   transmissivity feedback hypothesis during snowmelt, J. Hydrol., 219, 188–205, https://doi.org/10.1016/S0022-

650   1694(99)00059-1, 1999.

651   Kosugi, K., Fujimoto, M., Katsura, S., Kato, H., Sando, Y., and Mizuyama, T.: Localized bedrock aquifer

652   distribution explains discharge from a headwater catchment, Water Resour. Res., 47, W07111,
653   https://doi.org/10.1029/2010WR009884, 2011.

654 Martínez-Carreras, N., Hissler, C., Gourdol, L., Klaus, J., Juilleret, J., Iffly, J. F., and Pfister, L.: Storage controls on
655   the generation of double peak hydrographs in a forested headwater catchment, J. Hydrol., 543, 255–269,
656   https://doi.org/10.1016/j.jhydrol.2016.10.004, 2016.

657 McDonnell, J. J., Spence, C., Karran, D. J., Van Meerveld, H. J., and Harman, C. J.: Fill-and-spill: A process
658   description of runoff generation at the scale of the beholder, Water Resour. Res., 57, e2020WR027514,
659   https://doi.org/10.1029/2020WR027514, 2021.

660 McGuire, K. J., and McDonnell, J. J.: Hydrological connectivity of hillslopes and streams: characteristic time scales
661   and nonlinearities, Water Resour. Res., 46, W10530, https://doi.org/10.1029/2010WR009341, 2010.

662 Padilla, C., Onda, Y., and Iida, T.: Interaction between runoff–bedrock groundwater in a steep headwater catchment
663   underlain by sedimentary bedrock fractured by gravitational deformation, Hydrol. Process., 29, 4398–4412,
664   https://doi.org/10.1002/hyp.10498, 2015.

665 Penna, D., Tromp-van Meerveld, H. J., Gobbi, A., Borga, M., and Dalla Fontana, G.: The influence of soil moisture
666   on threshold runoff generation processes in an alpine headwater catchment, Hydrol. Earth Syst. Sci., 15, 689-
667   702, https://doi.org/10.5194/hess-15-689-2011, 2011.

668 Phillips, J. D.: Sources of nonlinearity and complexity in geomorphic systems, Prog. Phys. Geogr., 27, 1-23,
669   https://doi.org/10.1191/0309133303pp340ra, 2003.

670 Rinderer, M., van Meerveld, I., Stähli, M., and Seibert, J.: Is groundwater response timing in a pre-alpine catchment
671   controlled more by topography or by rainfall? Hydrol. Process., 30, 1036-1051,
672   https://doi.org/10.1002/hyp.10634, 2016.

673 Ross, C. A., Ali, G. A., Spence, C., and Courchesne, F.: Evaluating the Ubiquity of Thresholds in Rainfall‐Runoff
674   Response Across Contrasting Environments, Water Resour. Res., 57, e2020WR027498,
675   https://doi.org/10.1029/2020WR027498, 2021.

676 Sakakibara, K., and Suzuki, K.: Controlling Factors and Characteristics of Peak Runoff in an Alpine Headwater
677   Under the Asian Monsoon Climate, Mt. Res. Dev., 42, R1–R8, https://doi.org/10.1659/MRD-JOURNAL-D-
678   21-00030.1, 2022.

679 Scaife, C. I., and Band, L. E.: Nonstationarity in threshold response of stormflow in southern Appalachian headwater
680   catchments, Water Resour. Res., 53, 6579-6596, https://doi.org/10.1002/2017WR020376, 2017.

681 Scaife, C. I., Singh, N. K., Emanuel, R. E., Miniat, C. F., and Band, L. E.: Non-linear quickflow response as
682   indicators of runoff generation mechanisms, Hydrol. Process., 34, 2949–2964,
683   https://doi.org/10.1002/hyp.13780, 2020.

684 Sivapalan, M.: Process complexity at hillslope scale, process simplicity at watershed scale: Is there a connection,
685   Hydrol. Process., 17, 1037-1041, https://doi.org/10.1002/wrcr.20193, 2003.

686 Sloto, R. A., and Crouse, M. Y.: HYSEP: A computer program for streamflow hydrograph separation and analysis,
687   US Geol. Surv., https://doi.org/10.3133/wri964040, 1996.

688   Tian, F., Li, H., and Sivapalan, M.: Model diagnostic analysis of seasonal switching of runoff generation
689   mechanisms in the blue river basin, Oklahoma, J. Hydrol., 418-419, 136–149,
690   https://doi.org/10.1016/j.jhydrol.2010.03.011, 2012.

691   Tie, Q., Hu, H., Tian, F., and Holbrook, N. M.: Comparing different methods for determining forest
692   evapotranspiration and its components at multiple temporal scales, Sci. Total Environ., 633, 12–29,
693   https://doi.org/10.1016/j.scitotenv.2018.03.082, 2018.

694   Tromp-van Meerveld, H. J., and McDonnell, J. J.: Threshold relations in subsurface stormflow: 1. A 147-storm
695   analysis of the Panola hillslope, Water Resour. Res., 42, W02410, https://doi.org/10.1029/2004WR003778,
696   2006a.

697   Tromp-van Meerveld, H. J., and McDonnell, J. J.: Threshold relations in subsurface stormflow: 2. The fill and spill
698   hypothesis, Water Resour. Res., 42, W02411, https://doi.org/10.1029/2004WR003800, 2006b.

699   Uchida, T., Tromp-van Meerveld, I., and McDonnell, J. J.: The role of lateral pipe flow in hillslope runoff response:
700   an intercomparison of non-linear hillslope response, J. Hydrol., 311, 117-133,
701   https://doi.org/10.1016/j.jhydrol.2005.01.012, 2005.

702   Zhang, G., Cui, P., Gualtieri, C., Zhang, J., Bazai, N. A., Zhang, Z., Wang, J., Tang, J. B., Chen, R., and Lei, M.:
703   Stormflow generation in a humid forest watershed controlled by antecedent wetness and rainfall amounts, J.
704   Hydrol., 603, 127107, https://doi.org/10.1016/j.jhydrol.2021.127107, 2021.

705

706 **Appendix A:**

707
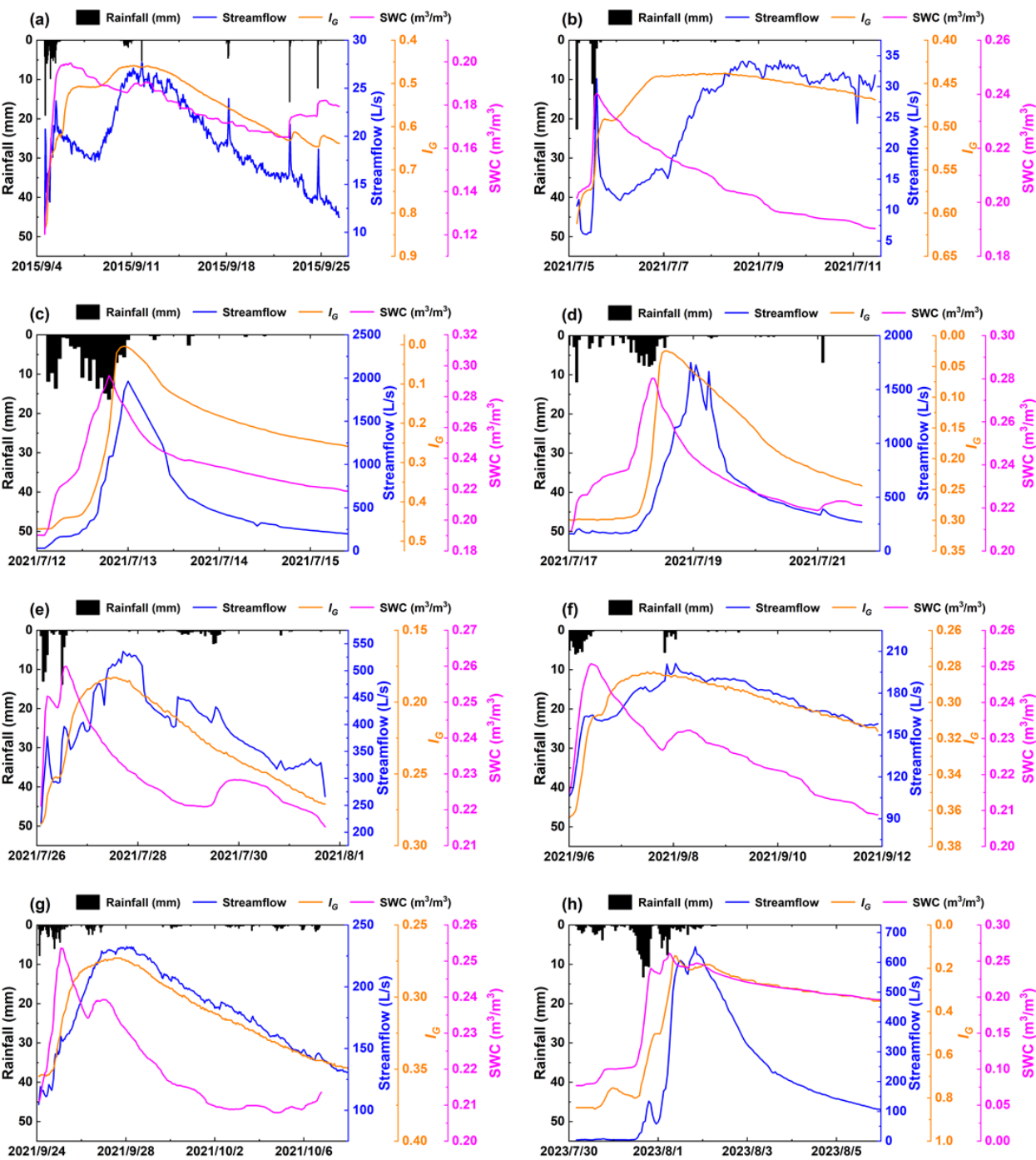
Figure A1. Examples of responses of streamflow, IG and soil water content to rainfall.